

## **Control of domain structure and magnetization reversal in thick Co/Pt multilayers**

Fallarino, L.; Oelschlägel, A.; Arregi, J. A.; Bashkatov, A.; Samad, F.; Böhm, B.;  
Chesnel, K.; Hellwig, O.;

Originally published:

January 2019

**Physical Review B 99(2019), 024431**

DOI: <https://doi.org/10.1103/PhysRevB.99.024431>

Perma-Link to Publication Repository of HZDR:

<https://www.hzdr.de/publications/Publ-28049>

Release of the secondary publication  
on the basis of the German Copyright Law § 38 Section 4.

# *Control of domain structure and magnetization reversal in thick Co/Pt multilayers*

L. Fallarino,<sup>1</sup> A. Oelschlägel,<sup>1</sup> J. A. Arregi,<sup>2</sup> A. Bashkatov,<sup>3</sup> F. Samad,<sup>4</sup> B. Böhm,<sup>4</sup> K. Chesnel,<sup>5</sup>  
and O. Hellwig<sup>1,4</sup>

<sup>1</sup>*Helmholtz-Zentrum Dresden-Rossendorf, Institute of Ion Beam Physics and Materials Research,  
Bautzner Landstrasse 400, 01328 Dresden, Germany.*

<sup>2</sup>*CEITEC BUT, Brno University of Technology, Purkyňova 123, 612 00 Brno, Czechia.*

<sup>3</sup>*Institute of Fluid Dynamics, Helmholtz-Zentrum Dresden-Rossendorf, Dresden, Germany.*

<sup>4</sup>*Institute of Physics, Chemnitz University of Technology, D-09107 Chemnitz, Germany.*

<sup>5</sup>*Department of Physics and Astronomy, Brigham Young University, USA.*

## *Abstract*

We present a study of the magnetic properties of  $[\text{Co}(3.0\text{ nm})/\text{Pt}(0.6\text{ nm})]_N$  multilayers as a function of Co/Pt bilayer repetitions  $N$ . Magnetometry investigation reveals that samples with high  $N$  exhibit two characteristic magnetization reversal mechanisms, giving rise to two different morphologies of the remanent domain pattern. For applied magnetic field angles near the in-plane field orientation, the magnetization reversal proceeds via a spontaneous instability of the uniform magnetic state resulting in perpendicular stripe domains. Conversely, for field angles close to the out-of-plane orientation, the reversal occurs via domain nucleation and propagation leading to a maze-like domain pattern at remanence. Our measurements further enable the characterization of the  $N$ -dependent energy balance between the magnetic anisotropy and magnetostatic energy contributions, revealing a gradual disappearance of the domain nucleation process during magnetization reversal for  $N < 14$ . This leads to the exclusive occurrence of an instability reversal mechanism for all field orientations as well as aligned-like stripe domains at remanence. Furthermore, a detailed study of the influence of the magnetic history allows the determination of a range of material properties and magnetic field strengths, where a lattice of bubble domains with remarkably high density is stabilized. These modulations of the ferromagnetic order parameter are found to strongly depend on  $N$ , in terms of center-to-center bubble distance as well as of bubble diameter. Moreover, such Co/Pt multilayers could be utilized to engineer field reconfigurable bubble domain lattices, which can resemble magnonic crystals.

# I. Introduction

Magnetic thin films with competing long and short-range interactions are a very important research topic in the field of ferromagnetism [1,2]. Due to their close competition, complex magnetization reversal processes as well as spatially inhomogeneous magnetic multi-domain states generally occur [3-13]. Undoubtedly, artificial layered structures consisting of alternating ferromagnetic (FM) / non-magnetic layers rightfully belong to this category [14-18]. In these systems, magnetocrystalline and surface anisotropies are typically opposing the magnetostatic self-interaction, causing the occurrence of heterogeneous microscopic magnetic states in order to minimize their total energy [17,19-21]. The resulting nanoscale magnetic textures have attracted significant interest due to their technological potential [22-28], as well as for their structural complexity [29-32]. In particular magnetic bubbles, which correspond to cylindrically shaped domains extending throughout the total thickness [33], were intensively studied largely motivated by their potential for applications in solid state storage [34,35]. While the industrial interest was pushed down by the subsequent advent of more efficient commercial devices [36], both the geometrical implication of magnetic bubble patterns and their dynamic behavior have become to a greater extent their primary research aspect [37-39]. As a matter of fact, a dipolar-stabilized bubble domain might be considered as a topological spin texture alike chiral skyrmions [40]. However, besides possible domain wall defects leading to achiral bubbles, the symmetric nature of dipolar interactions would lead to the co-existence of equal amounts of bubbles with both chiralities without the application of advanced patterning techniques together with specific magnetic field treatments [41].

Interestingly, by specific material parameter choices, the uniform ferromagnetic ground state can be established in artificial layered structures [42-44]. Therefore, a key issue in multilayer films is to find out under which conditions the system prefers spatial modulations of its FM order parameter instead of a simple homogeneous magnetic ground state, as well as to understand the mechanism governing the associated modulation period. The specifics of the resulting micromagnetic states are set by the relative strength of the competing interactions, whose ratio in multilayer structures can be tuned by changing for instance the individual layer thicknesses or the number of layer repetitions [17,45-47]. Moreover, while the energy balance is fixed by the material parameters, it was shown by Gao et al. [48] that the remanent magnetic

domain state configuration can be efficiently manipulated by applying an appropriate magnetic field routine leading to a highly dense remanent bubble-like domain lattice [49,50].

In the last two decades, an extensive work effort has led to an apparently very complete understanding of magnetization textures in magnetic multilayers [16,17,51,52]. The majority of these studies, though, utilized very thin FM layers, since an in-plane magnetization reorientation is expected for thicker films [47,53-55]. However, for sufficiently thick FM layers and in the presence of out-of-plane crystalline magnetic anisotropy, it was found that the magnetization undergoes a second reorientation transition back to out-of-plane orientation [6,12,13,30,56,57].

Based on the prior knowledge of FM multilayer thin films and our observations of various magnetic domain morphologies depending on magnetic history [49,50], the purpose of this paper is to provide an extensive exploration and description of their magnetization reversal as a function of the energy balance between magnetostatic and anisotropy energies. More importantly, the aim is to determine the existence of a specific energy ratio able to enhance the domain densities at remanence [48,49] while possibly stabilizing dense arrays of magnetic bubbles. This has been carried out by optimizing the total thickness of  $[\text{Co}(3.0\text{ nm})/\text{Pt}(0.6\text{ nm})]_N$  multilayers by varying the Co/Pt bilayer repetitions  $N$  in a range unexplored heretofore, in combination with finely adjusting the magnitude of the previously applied magnetic field.

Among the elemental ferromagnets, bulk Co adopts at room temperature the hexagonal close packed (*hcp*) crystal structure and possesses a magnetic easy axis (EA) along the *c*-axis. Thus, we have grown our multilayer films on top of a thick Pt (111) buffer layer such that Co grows with the necessary texture to induce an out-of-plane anisotropy-axis orientation. By studying in detail the influence of the magnetic history on the remanent domain pattern, and after having determined an optimal Co thickness leading to the formation of a bubble state [49], we find an optimal  $N$  for which a dense lattice of bubble domains is favored and the bubble density is maximized.

The paper is organized as follows. We describe specific experimental details in Section II. Then, in Section III A, the identification of the crystal structure and the evaluation of the epitaxial relationships are shown. In Section III B, the room temperature magnetometry characterization is presented and analyzed. The remanent magnetic states for various  $N$  including a magnetic domain density study as a function of the previously applied magnetic field are shown and discussed in Section III C-1. Section III C-2 describes the remanent magnetic state diagram of such multilayer

structures in terms of color coded-map. Finally, Section IV provides a summary of the accomplished results and general conclusions that can be drawn from our work.

## II. Methods

The  $[\text{Co}(3.0\text{nm})/\text{Pt}(0.6\text{nm})]_N$  multilayer (ML) films were prepared at room temperature by dc magnetron sputter deposition in an ultrahigh vacuum (UHV) system (ATC 2200 series from AJA International, Inc.) with a base pressure better than  $3 \times 10^{-6}$  Pa. Si substrates covered by a 100 nm thick thermal SiOx layer were used. For each layer, the deposition process was started only after pre-sputtering the targets for at least 30 s, using a pressure of  $4 \times 10^{-1}$  Pa of pure Ar atmosphere. As a template for the growth of (0001) textured *hcp* Co layers, a 1.5 nm Ta and subsequent 20 nm Pt layer were deposited using plasma power settings of 100 W and 30 W respectively. Thereafter, the Co and Pt depositions were performed by using 80 W and 30 W plasma powers respectively. Each sample was finally coated with a 2.3 nm thick Pt layer to avoid surface oxidation and contamination after removal from the vacuum system as well as aging effects. The Pt was also chosen as capping material to avoid breaking the spatial inversion symmetry along the out-of-plane (OOP) direction of the multilayer structure [58]. A schematic of the sample structure, including its specific layer sequence, is shown in Fig. 1(a) (top right part) together with the corresponding thicknesses. The structural analysis of the samples was performed by means of x-ray diffraction (XRD) and reflection (XRR) utilizing a Rigaku SmartLab x-ray Diffractometer with Cu-K $\alpha$  radiation. Magnetization measurements were performed using a commercial Microsense EZ7 vibrating sample magnetometer (VSM), equipped with a 360° rotational stage. Finally, magnetic domain imaging was performed via magnetic force microscopy (MFM) using a Bruker Multimode IV atomic force microscope and NSC18/Co-Cr/Al BS magnetic tips.

## III. Results and Discussion

### A. Structural characterization

In order to characterize the periodicity of the compositional modulation, we studied the crystallographic structure and the OOP mosaicity, for which XRR as well as XRD  $\theta$ -2 $\theta$  scans and rocking curve measurements were performed. Fig. 1(a) illustrates XRR  $\omega$ -2 $\theta$  scans in the angular range  $0.2^\circ \leq 2\theta \leq 9.0^\circ$  for the entire set of samples investigated in this study. Each measurement has been normalized to its maximum intensity and vertically offset by a constant value to permit

direct comparison. Interference-caused Kiessig oscillations with two different wavelengths are distinguishable in Fig. 1(a). A first type can be observed at low  $2\theta$  values, whose period is inversely proportional to the number of Co/Pt repetitions  $N$ . These short-wavelength oscillations correspond to the total thickness of the multilayers, since by increasing  $N$  (i.e. the total sample thickness) the distance in between two consecutive minima or maxima decreases. At the same time their relative intensity decreases while increasing  $N$ , due to the increasing number of interfaces as well as the absorption in each individual layer (whose number is  $2N$ ). In a wider  $2\theta$ -range a second set of Kiessig oscillations is noticeable, whose period ( $\Delta\theta \approx 0.2^\circ$ ) is constant as a function of  $N$ . They originate from the 20 nm thick Pt buffer layer, whose thickness is set to be constant independently of the sample. More importantly first and second order Bragg-like superstructure peaks, appearing at  $2\theta \approx 2.55^\circ$  and  $2\theta \approx 4.80^\circ$  respectively, have been measured for the entire set of our samples, giving a clear signature of a well-defined periodic elemental modulation of the multilayer structure independent of  $N$ . While it may be expected to observe superstructure peaks up to higher orders, the interfaces of any real multilayer system present slight imperfections due to roughness and interdiffusion. Such small deviations from perfect interfaces are partly responsible for the rapid reflectivity reduction of the intensities especially for higher order superstructure peaks as well as for the absolute broadening of their width. Moreover, due to the selected thickness of the individual layers, the higher order peaks are expected to be located at high angles  $2\theta$  where the reflected x-ray intensity has decreased rapidly with the inverse fourth power of the transferred wave vector magnitude [59]. Furthermore, the broadening of the individual ML-Bragg peaks is  $N$ -dependent: by increasing the number of Co/Pt bilayer repetitions, the width of the ML-Bragg peaks decreases substantially, as can be seen in Fig. 1(a). While this is partly caused by the sharpening of interference maxima with increasing  $N$  (analogously to the situation for diffraction gratings) as well as by the decreased overlap with Kiessig oscillations due to their reduced intensity and width, it can be furthermore notably linked to the stability of the Co/Pt bilayer thickness. Indeed, while increasing the number of Co/Pt bilayer blocks of constant total thickness  $t_{Co+Pt}$  within the experimental error, the individual  $t_{Co+Pt}$  should have a distribution getting closer and closer to a normal distribution where an angular broadening of the ML-Bragg peak decreases while increasing  $N$  [59]. Therefore, the observed evolution of the 1<sup>st</sup> and 2<sup>nd</sup> order full width at half-maximum (FWHM) peak value is importantly

confirming that the material parameters uniformity and reproducibility stay constant while increasing  $N$ .

Figs. 1(b) and (c) display XRD  $\theta$ - $2\theta$  scans in the angular range  $22^\circ \leq 2\theta \leq 102^\circ$  for all samples studied in this work, where the peak indexing in (c) refers also to (b). Similarly to the measurements in Fig. 1(a), each dataset has been normalized to its Si (400) diffraction peak intensity and is vertically offset by a constant value for direct comparison. All the scans look nearly identical in their overall appearance, exhibiting only well-defined diffraction peaks corresponding to Si (400), buffer Pt (111) and (222), Co/Pt (0002)/(111) and (0004)/(222) lattice planes<sup>1</sup>. The Pt buffer layer peaks look virtually the same for all samples, both in terms of angular position and FWHM, verifying the robustness of our fabrication process. This template layer stability allows us afterwards to ascribe any significant change in the magnetic properties to the specific number of repetitions  $N$  itself as opposed to inherent structural variations. Most relevantly, the entire set of samples exhibits a crystallographic orientation quality that is very similar to samples with individual thinner Co layers, despite the total thickness and high number of repetitions of the Co/Pt bilayer of the present study [46]. Thus, the total angular range shows only well-defined *fcc* (*nnn*) and *hcp* (000*l*) peaks for Pt and Co. The *hcp* lattice of Co was additionally verified via in-plane (IP) diffraction measurements, by setting the incident and diffracted beams nearly parallel to the sample surface, in which only Co (11 $\bar{2}$ 0) and (10 $\bar{1}$ 0) reflections were measured together with the one of Pt (220) for any sample studied in this work<sup>2</sup>.

Moreover, satellite peaks of the multilayer diffraction signals [indexed by  $n$  in Fig. 1(c)] have been measured, which are a clear indication of a perpendicular structural and material coherence far greater than the thickness of the individual layers. It can be also observed that the negative indexed satellite diffraction peaks have higher intensity than the positive ones, with the latter being within the noise level for  $n > 1$ . However, this effect is mainly caused by the overlapping and interfering waves coming from the  $-n$  satellite diffractions and the Pt (111) and Pt (222) diffraction planes. By using a triple Gaussian fitting function<sup>3</sup>, the positions of the 1<sup>st</sup> and 2<sup>nd</sup> order low angle Bragg-like superstructure peaks, displayed in Fig. 1(a), were evaluated in

---

<sup>1</sup> In Fig. 1(c) and in the text Co/Pt\* refers to Co (0002) / Pt (111), whereas Co/Pt\*\* to Co (0004) / Pt (222).

<sup>2</sup> However, our XRD-investigation cannot exclude the presence of *fcc* stacking faults.

<sup>3</sup> It was used a triple Gaussian function in order to take into account the superposition of left and right Kiessig oscillations coming from the total thickness and Pt buffer layer on the 1<sup>st</sup> and 2<sup>nd</sup> order Bragg peaks respectively.

order to estimate the average total thickness of the Co/Pt bilayer  $\bar{t}_{\text{Co+Pt}}$ <sup>4</sup>. Fig. 2(a) shows the  $N$ -dependence of  $\bar{t}_{\text{Co+Pt}}$ , where the errorbars correspond to the standard deviation values. Under the assumption of a purely statistical Gaussian distribution for the observed  $\bar{t}_{\text{Co+Pt}}$  values, all data fall into the interval defined by  $\bar{t}_{\text{Co+Pt}} \pm \sigma = 3.61 \pm 0.01$  nm, with  $\sigma$  being the standard deviation from the data average  $\bar{t}_{\text{Co+Pt}}$ . Indeed, the experimentally determined  $\bar{t}_{\text{Co+Pt}}$  is consistent within the statistically estimated error with the nominal total thickness value of 3.6 nm.

The average lattice constant of the Co/Pt bilayer was extracted from the angular positions of the Co/Pt\*<sup>1</sup> diffraction peaks in the  $\theta$ -2 $\theta$  scans, and plotted in Fig. 2(b) as a function of  $N$  together with the associated errors estimated from the least-squares Gaussian fit. The data are displayed along with reference values for bulk Pt (blue dashed line) and Co (red dotted line), for comparison. The lattice constants  $\bar{d}_{\text{Co+Pt}}$  shown in Fig. 2(b) correspond to the OOP interplanar distance of the superlattice-like cell consisting of both Co and Pt. Besides the absence of notable variations in between the extracted data, the values are consistently and substantially smaller than what one would expect for a Pt-rich superlattice cell or pure bulk Pt. The experimentally determined average value of  $\bar{d}_{\text{Co+Pt}} = 0.2089$  nm is only slightly larger than the corresponding weighted average thickness of 0.208 nm that is extracted from the of bulk parameters of Co/Pt multilayer structure parameters in this work. Furthermore, Fig. 2(b) reveals a slight trend towards smaller  $\bar{d}_{\text{Co+Pt}}$  values as  $N$  is increased. This effect could be caused by the initial strain from the 20 nm thick Pt buffer layer, which is stronger for less  $N$ .

In order to investigate the OOP crystallographic axis dispersion in the samples, rocking curve measurements have been performed for the Pt (111) and Co/Pt\* peaks<sup>1</sup>. The full widths at half maximum values of the peaks are plotted in Figs. 2(c) and (d) as a function of  $N$ , with the error-bars representing uncertainties estimated via the least-square Gaussian fits. Both sets of measurements indicate that the samples achieved remarkably good alignment of Co/Pt crystallographic  $c$ -axis orientation normal to the sample surface, when compared to previous works [60,61]. Finally, our structural sample analysis confirms the good crystallographic quality of the optimized layer growth sequence resulting in well-modulated Co/Pt multilayer films with

---

<sup>4</sup> Here, the average value refers to two independent averaging processes: one is directly connected to the volume averaged nature of the x-ray measurements, which is indeed dependent on the penetration depth of the beam as well as on its lateral extension; the second one is the arithmetic mean of the thicknesses calculated via the angular position of the 1<sup>st</sup> and 2<sup>nd</sup> order Bragg-like superstructure peaks at low angles.



perpendicular  $c$ -axis orientation, necessary for a preferential OOP orientation of the magnetization in such thick structures.

### *B. Magnetic characterization*

The macroscopic magnetic properties were analyzed to verify whether and how the designed multilayer structures exhibit a preferential orientation of their magnetization  $M$  parallel to the film normal. Figs. 3(a)-(m) present room temperature normalized  $M/M_{max}$  data as a function of the field strength  $\mu_0 H$  and number of Co/Pt bilayer repetitions  $N$ . For all hysteresis loops shown here, the (black) short dashed and (red) solid lines show the magnetization curves measured for an external magnetic field applied parallel and perpendicular to the film plane respectively. Fig. 3(a) shows the data for the thinnest sample in this study with  $N = 6$ . Despite the OOP orientation of the magnetocrystalline anisotropy axis, an in-plane behavior was found. The measurement shows an almost perfectly rectangular-shaped hysteresis for the IP applied field with an abrupt magnetization reversal. In contrast, the OOP field data in Fig. 3(a) show an almost completely reversible change in the magnetization orientation where the complete alignment is reached only at a field strength of  $\mu_0 H_S^{OOP} \approx 1.3$  T. The small hysteresis effect during the OOP reversal process is the result of slight sample imperfections. At the other end of our sample spectrum, Fig. 3(m) shows two reversal curves that are a clear indication of OOP preferential orientation of the magnetization [6,7,17]. For  $\mu_0 |H| > \mu_0 H_S^{OOP} \approx 1.15$  T, the system exhibits in both geometries a uniform magnetization state parallel to the field direction. In the IP field case the saturated state becomes unstable at the critical field  $\mu_0 |H_{cr}| \approx 0.5$  T upon reducing the field strength, and undergoes laterally alternating magnetization rotations driven by the magnetocrystalline OOP anisotropy culminating in the formation of a remanent stripe domain configuration. However, an IP magnetization component persists at remanence mainly within the domain walls, which is aligned during the field sequence and which is responsible for the hysteresis that occurs for low field values [6-8]. For the OOP field configuration, once the field is lowered, the uniform state is altered by the formation of bubble domains with opposite magnetization orientation driven by magnetostatic energy. This process starts rather abruptly at the nucleation field  $\mu_0 |H_n^{OOP}| \approx 1$  T, leading to a sharp drop in the magnetization. As the field is further reduced the domain dimensions increase resulting in the linear field dependence of the magnetization down to remanence. The observed small hysteresis effect is again the result of slight sample imperfections [62].

From our experimental data in Fig. 3, we concluded that  $N$  has a profound impact on the magnetization reversal characteristics of thick Co/Pt multilayers. While the overall appearance of the IP and OOP magnetization reversal curves stays very similar for  $16 \leq N \leq 30$  [Figs. 3(f)-(m)], an appreciable change occurs in the two OOP-hysteretic regions at high field magnitudes, associated with the nucleation and annihilation of domains. In fact, upon increasing  $N$ , their position along the magnetic field axis shifts to progressively higher values as well as their area becomes gradually larger. This is evidenced in the close-up plots shown in Figs. 3(n)-(q). Differently, by decreasing  $N$  below 14, these hysteretic areas collapse entirely as displayed in Fig. 3(d). In contrast to this change in the nucleation behavior, the central hysteresis does not disappear, but instead actually increases significantly between  $N = 14$  and  $N = 10$  for OOP field orientation, before it decreases again for even smaller  $N$ , consistent with previous observations in pure Co systems when decreasing the effective OOP anisotropy [6,13]. Also,  $M_S$  maintains a nearly constant value in the entire  $N$ -range studied. The OOP saturation field  $\mu_0 H_S^{\text{OOP}}$ , the nucleation field  $\mu_0 H_n^{\text{OOP}}$ , and the IP saturation field  $\mu_0 H_S^{\text{IP}}$  strengths are plotted as a function of  $N$  in Figs. 3(r) and (s). The  $\mu_0 H_S^{\text{OOP}}(N)$  data can be divided into two branches that join in a cusp-like point located at  $N = 14$ . For  $N \geq 14$  the OOP saturation field monotonically increases while increasing  $N$  and hence the sample thickness, as already predicted by Thiele [33] and experimentally measured by Hehn et al. [7] for a single magnetic film with OOP anisotropy. On the contrary, for  $N < 14$ ,  $\mu_0 H_S^{\text{OOP}}$  monotonically increases when reducing  $N$ .

Based on the behavior of the OOP loops and corresponding saturation fields, three different  $N$ -ranges can be identified in which the magnetic state before OOP saturation and the mechanism for reaching the saturated single domain state at  $\mu_0 H_S^{\text{OOP}}$  are fundamentally different: (i) for  $N > 14$ , before OOP saturation the sample consists of magnetic bubbles which collapse upon reaching  $\mu_0 H_S^{\text{OOP}}$ ; (ii) in the interval  $10 \leq N < 14$ ,  $\mu_0 H_S^{\text{OOP}}$  describes the field at which the laterally alternating non-uniform magnetization state vanishes in favor of a uniform magnetic state; (iii) and for  $N < 10$ , reaching OOP saturation refers to the process during which the magnetization vector continuously rotates from the easy plane direction towards the OOP field direction. Differently, both  $\mu_0 H_S^{\text{IP}}$  and  $\mu_0 H_n^{\text{OOP}}$  increase their values monotonically with  $N$ . The  $\mu_0 H_S^{\text{IP}}$  evolution is mainly driven by the increase of the OOP effective anisotropy while increasing the total thickness of the investigated samples, as already observed in previous studies on single

Co thick layer [6,7]. The  $N$ -dependence of  $\mu_0 H_n^{\text{OOP}}$  is directly related to the total thickness of the systems, for the nucleation field being a growing function of the film thickness [6,33].

As seen in Fig. 3, our multilayer samples show fundamentally different magnetization reversal processes while applying the magnetic field along in- and out-of-plane directions and by varying  $N$ . As a result, in order to fully magnetically characterize this kind of system, not only IP and OOP orientations of the magnetic field should be explored, but also any intermediate field angles. In order to perform this angular dependent study, a convenient methodology introduced in earlier studies was utilized [12,13], which takes advantage of the normalized magnetization difference  $\Delta M/M_{\text{max}}$  between the ascending and descending branches of the magnetization curves. Correspondingly,  $M(H)$  curves have been measured for different applied field orientations<sup>5</sup>  $\beta$ , in steps of  $\Delta\beta = 5^\circ$  for  $30^\circ \leq \beta \leq 95^\circ$ , and  $\Delta\beta = 2^\circ$  for  $-30^\circ \leq \beta \leq 28^\circ$ . The complete angular dependence of the normalized magnetization difference is shown in Fig. 4 as a color-coded maps of  $\Delta M/M_{\text{max}}(\beta, H)$  in the  $8 \leq N \leq 30$  Co/Pt bilayer repetitions range<sup>6</sup>. As it can be clearly seen, the resulting  $\Delta M/M_{\text{max}}(\beta, H)$  maps strongly depend on  $N$ , showing significant changes especially in the high magnetic field regime. For  $N = 30$ , the low magnetic field hysteresis forms a central band that extends from left to right over all magnetic field angles, even though it decreases in width near  $\beta = 0^\circ$ . In contrast, the domain nucleation hysteresis is visible in this plot via the presence of two non-zero  $\Delta M/M_{\text{max}}$  value regions centered at  $\mu_0 H \approx \pm 1$  T and  $\beta = 0^\circ$ . Upon changing  $\beta$  away from the OOP orientation, the width of these regions in field gradually reduces, and they completely disappear for  $\beta > 10^\circ$  or  $\beta < -10^\circ$ . Hence we can conclude that for orientation  $\beta < -10^\circ$  and  $\beta > 10^\circ$  the magnetization reverses by undergoing a second-order rather than a first-order phase transition [12,13]. On the contrary, the color-coded map for  $N = 8$  (Fig. 4) is characterized by the sole existence of a central hysteresis band, showing a slight increase near the OOP field orientation ( $\beta = 0^\circ$ ). Therefore, we see that by varying the total magnetic thickness of the multilayer system, there is a threshold minimum total magnetic thickness ( $N \times t_{\text{Co}}$ ) for which hysteretic nucleation (and annihilation) of perpendicular bubbles and stripe domains occurs, a process indicated by the existence of non-zero  $\Delta M/M_{\text{max}}$  regions outside the central band and near the OOP field orientation. Without dramatically changing in field position, their angular extension shrinks progressively upon decreasing  $N$ , down to the point where they collapse

<sup>5</sup>  $\beta = 0^\circ$  corresponds to  $H$  applied along the surface normal,  $\beta = 90^\circ$  refers to in-plane field orientation.

<sup>6</sup> The sample  $N = 6$  is not further investigated due to its similarity with respect to  $N = 8$ .

entirely. In contrast to this change in the nucleation behavior, the central hysteresis band does not disappear, but instead increases. Analogous to the situation earlier observed in thick (0001) oriented Co-films [12,13], the angular extension of the nucleation process is controlled by the evolution of the  $\mu_0 H_{cr}(\beta)$  and  $\mu_0 H_n(\beta)$  curves and by their complete different angular dependence that produces a crossing at a specific  $\beta$ . By reducing the ratio between anisotropy and magnetostatic energy in favor of the latter, which was achieved for instance in Ref. 13 by increasing the temperature of pure single Co films, the angular position of the crossing point shifts towards  $\beta = 0^\circ$  until its complete suppression. Thus the experimental observations in Fig. 4 reflect the thickness-induced variations of the  $(\beta, \mu_0 H)$  regions where each of the two magnetization reversal mechanisms dominate for our Co/Pt multilayers, as a result of the inherent thickness dependent ratio of magnetic anisotropy and magnetostatic energies. In fact by reducing  $N$  (i.e. the total magnetic thickness), the crossing point between the two reversal mechanisms is gradually shifting to lower  $\beta$  values until disappearing, which implies that the instability reversal process then occurs for any angle of the externally applied field.

In order to better visualize the energy-ratio dependence of the reversal mechanism, the same datasets shown in Fig. 4 were plotted and magnified for the extreme cases of  $\beta = 0^\circ$  and  $90^\circ$  (OOP and IP, respectively), displayed in Fig. 5. For the OOP geometry [Fig. 5(a)] we can recognize two characteristics bands of non-zero  $\Delta M/M_{max}$  value near applied fields of  $\pm 1$  T for high  $N$  values. As  $N$  is decreased from 30, an initial gradual reduction in field position of the two nucleation regions is followed by their complete disappearance for  $N < 14$ . Differently, the central band stays nearly constant down to  $N = 14$ , where it starts to expand significantly before shrinking again at the lowest Co/Pt bilayer repetition used in our experiments. For the IP configuration, Fig. 5(b), a gradual reduction of the central hysteretic band with decreasing  $N$  is visible without the appearance of any other hysteretic structure in the entire  $N$ -range. This behavior is fully consistent with the high field hysteresis-free phase transition from a uniform state into an instability induced stripe domain pattern. This leads to a hysteresis peak around zero field due to the existence of a net IP magnetization component (within the domain walls) for this state. By associating the existence of the high field hysteretic behavior with nucleation and the absence of it with instability-driven stripe domain generation, Fig. 5 implies that for  $N < 14$  the latter extends to every applied magnetic field angle.

However, an important aspect has still been neglected in our discussion. While lowering the number of bilayer repetitions from  $N = 30$ , our samples are also experiencing a thickness-induced magnetization reorientation transition that culminates at the lowest studied  $N$ -value with a reversal mechanism characterized by IP magnetization states alone [6,30,57]. In fact, the IP magnetization reversal curves displayed in Figs. 3(a) and (b) have lost the strong curvature of the high  $N$ -samples loops and exhibit almost full remanent magnetization. Thus, the samples with  $N \leq 8$  are evidently in an IP magnetization state at remanence, as it will be seen and further discussed in conjunction with Figs. 6 and 7. Importantly, the magnetization reversal evolution as a function of  $N$  must have a direct impact on the remanent magnetic domain state for those samples with high repetition number  $N$ , enabling its manipulation in terms of modulation period and microstructure by applying specific magnetic field sequences. Therefore, character and tunability of the remanent magnetic domain structures have been investigated via MFM measurements in the next section.

### C. MFM characterization

#### 1. *Characteristic domain patterns*

The magnetometry characterization illustrates that qualitatively different magnetization reversal behaviors can emerge from the different balance between the magnetic anisotropy and magnetostatic energy contributions, which can be tuned in our thick multilayer films by means of varying  $N$ . The absence of the nucleation phase at low  $N$  was identified across the entire  $H$ - $\beta$  parameter space upon analyzing the color-coded maps in Figs. 4 and 5 [13]. In order to confirm the physical picture deduced from our VSM data, the remanent domain patterns were measured via MFM. For samples with  $N < 14$ , we aim towards validating the persistence of a sufficiently large anisotropy able to support a stripe domain state at remanence, despite the disappearance of the nucleation type hysteresis earlier found. For this purpose, the magnetic configuration was brought as close as possible to the equilibrium state in the OOP reference system by demagnetizing it, i.e. by applying an oscillating field of decreasing amplitude starting above  $\mu_0 H_S^{\text{OOP}}$ . Fig. 6 shows the corresponding remanent (demagnetized) MFM images recorded after the described OOP demagnetization process as a function of  $N$ . At large thicknesses ( $N \geq 18$ ), the magnetic configuration consists of a disordered array of stripes with well-defined widths. The corresponding maze-like domain pattern is the result of the heterogeneous nucleation and expansion of bubble domains, which develops randomly due to the symmetry breaking caused by

the nucleation process at  $\mu_0 H_n^{\text{OOP}}$ . Opposite to this, when looking at the MFM images for lower multilayer thicknesses ( $10 \leq N \leq 16$ ), the magnetic pattern is more ordered possessing a well-defined domain period. Indeed, for  $N = 10$ , the perpendicular magnetization component is still found to have a periodic OOP up and down magnetization modulation, as confirmed by the weakly striped MFM contrast. Even though the magnetization is coherently aligned along the stripes axis, it should not have in principle a preferential IP direction (opposite to the case of a film with IP uniaxial anisotropy [63,64]), because the stripe orientation is not fixed but instead depends on the sample history. However, for our samples with small  $N$  values, a preferential direction along which the stripes align can be readily observed. We suggest that this is mainly triggered by the gradual extension to any magnetic field application angle  $\beta$  of the instability-driven stripe domain generation, suppressing any level of disorder that the nucleation of bubbles may introduce (that for  $N=14$  and  $16$  occurs only  $-2^\circ \leq \beta \leq 2^\circ$  as depicted in Fig 4). Therefore, the whole stripe pattern orders parallel to the last experienced saturation field or, as in this case, to the direction of the small IP field component arising from possible experimental misalignment between the direction of application of  $\mu_0 H$  and the sample surface normal. This attributes an oriented and “rotatable” IP anisotropy to the multilayer films with low  $N$  despite OOP application of  $\mu_0 H$  [65]: by changing the misalignment angle of the externally applied magnetic field during the demagnetization process, the small IP component would rotate accordingly on the sample surface plane. This induces a preferential axis for the stripe domains, due to the tilt of the stripe domain magnetization in the direction of the fields IP component and the associated Zeeman energy gain for an alignment of the stripes in this direction. Note that this behavior is not observed in samples with high  $N$ , due to the higher effective OOP anisotropy respectively in-plane saturation field, leading to a much less tilted magnetization in an external field with small IP component. Finally, as the perpendicular magnetization curve obtained for the  $N = 6$  and  $N = 8$  are characteristic for a film with IP magnetization, the corresponding MFM image for  $N = 8$  displayed in Fig. 6 shows large IP domains with typical widths over  $1 \mu\text{m}$ . The two-dimensional Fast Fourier Transformation (2D-FFT) analysis taken over each large scan-size MFM images ( $10 \times 10 \mu\text{m}^2$ ) confirms the  $N$ -dependent directionality of the stripe domains alignment. Decreasing the number of Co/Pt repetitions  $N$  causes the symmetric circle-like high intensity region gradually to break into two separated “quarter moon-like” structures.

In addition, we have studied the remanent domain patterns after IP demagnetization process. Fig. 7(a) and (b) shows MFM images for samples with  $N = 30$  and  $N = 10$  respectively. The alignment of the parallel component of the magnetization with the field, in order to minimize the Zeeman energy, leads to periodic patterns of parallel stripes for all samples between  $30 \geq N \geq 10$ , as already predicted and confirmed experimentally for similar total thicknesses [6,66]. Although the investigated systems have a complicated magnetic behavior, the stripe domain state is generally accepted as the energetically preferred state in the absence of an applied magnetic field. Thus in Figs. 7(a) and (b) the symmetry breaking along the IP direction forces the stripe walls and stripes themselves to align along one direction, whereas in the case of OOP-demagnetization process and in the presence of nucleation hysteresis only the local order is preserved and the free-energy minimization as well as the finite temperature at which the experiment has been carried out lead to globally disordered patterns. However, we have seen that the disorder is suppressed while reducing the ratio between anisotropies and magnetostatic energies as shown in Fig. 6 for  $10 \leq N \leq 14$ . In this  $N$ -range the remanent domain state after a full demagnetization process shows an aligned stripe domain pattern independent of the alternating magnetic field orientation (except in the case of a virtually perfect OOP field alignment).

In order to evaluate the dependency of the domain size on  $N$  (or on the total magnetic thickness), 2D-FFT of the MFM images after an IP demagnetization process were calculated using periodic boundary conditions. Linear profiles crossing  $k(0,0)$  were then extracted in order to evaluate the domain periodicity  $\lambda$ , with the spatial frequency  $k_0$  ( $\mu\text{m}^{-1}$ ) being defined as the center of the fit to a Gaussian curve as well the deviation  $\Delta k_0$  ( $\mu\text{m}^{-1}$ ) in terms of its FWHM. Fig. 7(c) displays the domain periods  $\lambda$  as a function of Co/Pt bilayer repetition, where  $\lambda$  increases for as  $\propto \sqrt{N}$  in accordance with Kittel's law for stripe domains [2,30]. The red line in Fig. 7(c) corresponds to the fitting results obtained by using a power-law function with exponent  $1/2$ .

An additional feature that is visible in Figs. 6 and 7 consists in that the MFM domain contrast is also  $N$ -dependent, dramatically decreasing with  $N$ . This effect is mainly driven by the canting of the local magnetization induced by the IP reorientation for low  $N$ . Such a canting angle varies monotonously with  $N$  as indicated by the  $N$ -dependence of the in-plane remanence ratio  $M_r^{IP}/M_{max}^{IP}$  shown in Fig. 7(d). Samples with  $N > 20$  exhibit a low IP remanence, arising mainly from the local magnetic moments confined inside the domain walls. This gradually increases when lowering  $N$  in the intermediate range ( $10 \leq N \leq 20$ ), indicating a canting of the domain

magnetization towards the film plane. This behavior is in agreement with the appearance of the two low intensity regions along the otherwise high intensity rings into the 2D-FFT color-coded maps shown as insets in Fig. 6. Finally, for  $N < 10$ , the magnetization is fully in plane as indicated by the MFM images in Fig. 6. Similar observations of a thickness driven reorientation of the magnetization from IP to OOP (and vice versa) have been reported for numerous systems, including (0001) oriented Co films [5,6] as well as in multilayer structures with ultrathin bilayer units [67,68].

In summary, we see that the applied field orientation  $\beta$  as well as the balance of magnetic energy contributions have a significant impact on the morphology of the remanent domain states: a full demagnetization processes may result in either aligned or randomly distributed stripe domain patterns, by simply changing either  $\beta$  or  $N$ . In the next section, we explore the viability of modulating the remanent magnetic domain configuration via minor loop cycling, as suggested in prior studies [48-50].

## 2. Manipulation of domain shapes

Next, we aim towards achieving control of the remanent magnetic domain pattern structure in our  $[\text{Co/Pt}]_N$  multilayers via minor loop cycling with the field applied along the OOP orientation. For this, a descending series of minor loops was applied to the sample with MFM images taken in between. Fig. 8(a) shows as (red) line normalized  $M/M_{\text{max}}$  as a function of the positive reduced field  $h = \mu_0 H / \mu_0 H_S^{\text{OOP}}$  data for the sample  $N = 20$ , with  $\mu_0 H_S^{\text{OOP}}$  being the OOP saturation field. The inset displays the MFM image<sup>7</sup> of the remanent magnetic state after applying the maximum reduced field  $h_m = 1.6$ . The resulting domain pattern is already quite different from the MFM image measured after the full OOP demagnetization process (Fig. 6). Indeed, the MFM measurement displayed in the inset of Fig. 8(a) is reminiscent of the elliptic bubble domains predicted by Thiele [33], consisting of randomly distributed short stripe domains. The absence of any global alignment is due to the external field possessing no significant IP component as well as its maximum strength being larger than  $\mu_0 H_S^{\text{OOP}}$  in the presence of nucleation hysteresis at high field. The remanent domain pattern established after applying  $h_m = 1.6$  has been selected as the

---

<sup>7</sup> The MFM images displayed in Fig. 8 have been measured on different region of the samples, i.e., they do not correspond to the same sample area.



starting point for the entire minor loop investigations of each sample<sup>8</sup>. Setting  $h_m = 1$ , the corresponding normalized magnetization curve plotted in Fig. 8(b) shows that the reversal still occurs as a first-order phase transition via nucleation of reverse domains. The inset shows the evolution of the remanent domain structure, in which some short stripes have split into bubble-like domains. By further decreasing the reduced field strength to  $h_m = 0.95$ , as shown in Fig. 8(c), the magnetization reversal curve does not show the first order reversal behavior anymore, indicating that the magnetization mechanism here is mainly occurring via domain wall motion. By describing the curve along the ascending part, the domains magnetized opposite with respect to the external field get linearly smaller in width to form disordered stripes while increasing  $h$ , before splitting in their length at sufficiently high field, thus transforming into isolated bubbles. By then decreasing the field back to  $h = 0$ , the magnetic state consisting of bubbles and short stripes at  $h = h_m$  is imprinted in the remanent domain pattern as noticeable in the inset of Fig. 8(c). This is due to the magnetostatic repulsion of the presumably high density of domains at  $h_m$ , preventing them from merging to extended stripe domains.

In order to further investigate the effect of magnetic history on the remanent domain morphology, and in an attempt to better target the optimal field value  $h_m$  maximizing the magnetic domain density, a series of MFM images at remanence were measured after applying one complete magnetization loop of amplitude  $h_m$ . The amplitude  $h_m$  was progressively decreased in steps of 0.05 down to 0.6 for each sample. For comparison between datasets, the tip-sample distance was fixed at 40 nm and the color-code scale fixed at  $0.5^\circ$  (phase shift) in all MFM measurements. The signal contrasts of different remanent state images exhibit no change, which means that the intensity of the surface stray field has also not changed within each sample. As visible in Figs. 8(d)-(f), while the  $h_m$  values are confined in a field range corresponding to the nucleation hysteresis of the major loop, by decreasing the minor loop amplitude the shortened stripes collapse into bubbles arranging themselves into a quasi-hexagonal lattice as indicated in the top-left inset of Fig. 8(f). By further decreasing  $h_m$ , the minor loop extension slowly recedes from the nucleation hysteresis of the major loop, and consequently less stripe domains reach a

---

<sup>8</sup> Each minor magnetization loop was performed in the following way: starting from remanence ( $h=0$ , after having performed a full major magnetization loop) the field strength is first increased to its maximum value  $h_m$ , then reversed down to  $-h_m$ , increased up again to  $h_m$  and finally reduced back to 0. At this last point the remanent MFM images were recorded.

sufficient opposite magnetic field in order to pinch into bubble domains and thus are preserving the stripes-like geometry at remanence, as shown in Figs. 8(g) and (h).

Considering the MFM images displayed in Figs. 6 and 7, we can expect that the magnetic domain period as well as its morphology is determined by the long-range and short-range competing interactions, whose ratio is varied by changing  $N$ . Moreover, the minimum diameter of individual bubbles as well as its ratio with respect to its domain wall width strongly depend on the balance between anisotropy and the magnetostatic energies [33,40]. Therefore, in order to further explore the formation of a bubble lattice at room temperature, the above described minor loop investigation has been performed as a function of the number of Co/Pt repetitions  $N$  to investigate the role of the thin film magnetostatic energy for the modulated phase. Fig. 9 shows the full remanent MFM characterization for the samples with  $14 \leq N \leq 30$  as a function of the reduced field  $h_m$ . The samples with small  $N$  were excluded from this investigation due to the absence of a first order nucleation of domains, which should prevent the formation of isolated domains at remanence.

The choice of  $N$  and  $h_m$  has a profound impact on the remanent domain pattern morphology, thus setting up a way for the effective manipulation of high-density bubble-like domain lattices. We find the field range of  $0.70 \leq h_m \leq 0.85$  to be the optimal setting in order to stabilize remanent domain patterns which consist of bubble-like shaped domains, whereas for higher and lower  $h_m$  those domains tend to interconnect into more elongated stripes. However, the samples with a low number of Co/Pt repetitions  $N$  (especially  $N = 14$ ) even in the optimal magnetic field range, exhibit a majority of domains adopting a stripe-like shape instead of the bubble-like. The observation of an increased number of elongated domains while decreasing  $N$  at a fixed valued of  $h_m$  is mainly caused by a thickness driven reorientation transition towards an easy-plane behavior, as it was observed when analyzing the VSM data. Therefore, for small  $N$ , slight misalignments of the magnetic field direction with the OOP orientation introduces, as corroborated in Fig. 6, a preferential IP direction along which the domain patterns align. In the case of Co/Pt multilayers with higher  $N$  values, decreasing  $h_m$  below the nucleation hysteretic field range causes the number of stripe-like domains to increase substantially as can be seen in Fig. 9 for  $h_m < 0.7$  and  $20 \leq N \leq 30$ . Indeed, by performing a full demagnetization process, i.e.  $h_m = 0$ , all isolated magnetic domains merge into very-long connected domains that form a maze-like pattern, as displayed in Fig. 6.

For all measurements in Fig. 9, we defined the remanent domain density  $\rho$  as the number of domains per  $100 \mu\text{m}^2$  area. Calculated values of  $\rho$  are indicated within the inset of the MFM images shown in Fig. 9, where  $\rho$  values are seen to range in about an order of magnitude, between 200 and more than 2000. In addition, the specific dependence of  $\rho$  on  $h_m$  is displayed in Fig. 10 for samples with  $N \geq 14$ . For all samples shown here, the density of domains for  $h_m < 0.5$  is relatively small; however, by further increasing  $h_m$ ,  $\rho$  increases significantly up to its maximum value  $\rho_{\text{max}}$ . Beyond this point, the density decreases again and reaches values close to zero at and above saturation for low  $N \leq 16$  [Figs. 10(a) - (b)], but keeps high offset values for  $N \geq 18$  [Figs. 10(c) - (i)]. Indeed, as the inset MFM images in Figs. 10(a) - (i) show for  $h_m = 1.6$ , the remanent domain pattern consists of very long stripe domains for  $N = 14$  and 16 showing a zigzag structure that might be induced due to magnetic tensile strain originating from the slight misalignment of the magnetic field direction with respect to the surface normal [11]. Nevertheless, for  $N \geq 18$ , the remanent domain patterns for  $h_m = 1.6$  are characterized by a mixed state made of short stripes and bubbles, whose density increases considerably with respect to the low- $N$  cases. This change of the remanent domain pattern after applying  $h_m > 1$  can be ascribed to the IP reorientation transition occurring for samples with  $N \leq 18$ . A considerable in-plane component of the magnetization may be responsible for the increased length of domains and consequently for the change in their morphology.

The optimal reduced field stabilizing the highest density of domains at remanence was determined by fitting the experimental data in Figs. 10 (a)-(i) to the bi-Gaussian function:

$$\begin{aligned} \rho &= \rho_{0_1} + A_1 e^{-\frac{(h-h_{\text{max}})^2}{2w_1^2}} & h \leq h_{\text{max}} \\ \rho &= \rho_{0_2} + A_2 e^{-\frac{(h-h_{\text{max}})^2}{2w_2^2}} & h_{\text{max}} \leq h \end{aligned} \quad (1)$$

with  $h_{\text{max}}$  being the reduced field at which the highest density is found. Hereby, the offsets  $\rho_{0_i}$ , the peak widths  $w_i$ , the scaling factor  $A_i$  ( $i=1, 2$ ) and  $h_{\text{max}}$  were utilized as fit parameters, with the constrain  $\rho_{0_1} + A_1 = \rho_{0_2} + A_2$  (continuity at the peak). Figs. 10 (a)-(i) shows the fitting results as red solid lines in direct comparison to the experimental data. In each case, an excellent agreement has been found between the experimental data and the least-squares fit according to Eq. (1). The extracted values for  $h_{\text{max}}$  together with the associated errors estimated from the fits are shown in Fig. 10(j) as a function of  $N$ . Despite small variations in between the extracted optimal reduced

fields for the samples, all  $h_{max}$  values are consistent within their average value  $\bar{h}_{max} = 0.80 \pm 0.07$  that has been determined from the experiments and in agreement with earlier estimates for  $N = 50$  [49].

With the purpose of summarizing our experimental results in a global picture, we have used the maximum density values  $\rho_{max}$  extracted from the MFM images in Fig. 9 in order to build a  $N$ - $h_m$  remanent state phase diagram, which illustrates the measured magnetic domain densities at remanence. In the density map, which is displayed as a color-coded plot in Fig. 11(a), the maximum domain density for any investigated sample is reached in the region  $0.70 \leq h_m \leq 0.85$ . Moreover, it can be clearly seen that the maximum domain density is observed for  $18 \leq N \leq 20$ . In fact, the maximum value  $\rho_{max}$  is observed for  $(N, h_m) = (18, 0.80)$ , where we have obtained a value of  $2274 \pm 160$  domains per  $100 \mu\text{m}^2$ . In addition, there are two predominant magnetic configurations that consist of stripes and bubbles. The former configuration changes its morphology depending on the number of Co/Pt repetitions, because of the change in the energy landscape. For both high  $N$  and  $h_m$ , the samples show at remanence short stripe domains whereas by substantially decreasing the reduced field the domains increase their length forming labyrinth domains. On the other hand, for low  $N$  values, canted short stripe domains have been measured for a large range of  $h_m$  strength. Importantly, the region of the map with the highest number of domains corresponds in majority to bubbles. In fact, our phase diagram in Fig. 11(a) suggests that the morphological stripe-bubble magnetic transition is accompanied by a significant enhancement in the domain density. In Fig. 11(b), the maximum density  $\rho_{max}$  is plotted as a function of  $N$ . From here, one can observe that when the number of Co/Pt repetitions approaches  $18 \leq N \leq 20$ , the domain density at remanence maximizes. By combining our experimental data with that in Ref. 49, a more complete  $t_{Co}$  -  $N$  color-coded domain density map can be constructed, which is shown as a color coded map in Fig. 11(c). At the fixed number of Co/Pt repetitions  $N = 50$ , a strong increase of the remanent domain density at a thickness of  $t_{Co} \sim 3$  nm corresponding to 1200 domains per  $100 \mu\text{m}^2$  was found [49]. However, one can additionally see from the outcome of our experiments that via decreasing the number of Co/Pt repetitions, the density of domains can be further increased up to the value of  $\rho = 2274 \pm 160$  domains per  $100 \mu\text{m}^2$  for  $N = 18$  [see Fig. 11(b)]. As previously pointed out, the domain density decreases again for  $N < 18$ , as a result of the gradual IP reorientation transition of magnetization.

Finally, we have also estimated the fundamental length scales of the bubble-like domain lattices stabilized in our  $[\text{Co/Pt}]_N$  multilayers. Fig. 11(d) displays the characteristic nearest neighbor distance  $D$  between bubbles as a function of the average bubble radius  $r$ , the definition of both being schematically defined in the inset of the figure. We see that by reducing the number of Co/Pt repetitions, the average bubble radius decreases monotonically, in good agreement with previous findings on garnet systems [69]. This property allows the system to arrange more and more bubbles along a given line by reducing their peak-to-peak distance  $D$ . Also the estimate of the bubble size at  $N = 50$  (radius of about 75 nm [49]) agrees well with the trend shown on Fig. 11 (d).

## IV. Conclusions

In this paper, we have successfully fabricated  $[\text{Co}(3.0\text{nm})/\text{Pt}(0.6\text{nm})]_N$  multilayer films with a magnetic easy axis perpendicular to the film plane and narrow  $c$ -axis dispersion. The room temperature magnetometry measurements for the sample with  $N = 30$  reveal the presence of two very different magnetization reversal processes depending on the applied field angle  $\beta$ , namely an instability-driven process leading to the generation of stripe domains for  $\beta$  values near IP field orientation and a nucleation domain process near OOP field orientation that is hysteretic in nature. Our  $N$ -dependent study shows a gradual shrinking of the nucleation regime, so that at sufficiently low  $N$  only the instability-driven second-order phase transition occurs for all angles  $\beta$ . The disappearance of the nucleation regime is driven by the strong thickness dependent balance between magnetic anisotropy and magnetostatic energies and occurs before the effective OOP anisotropy energy becomes too weak to support a stripe domain state altogether, i.e. it occurs while the stripe domain instability is still dominating the magnetization reversal process. By further reducing the number of Co/Pt repetitions below  $N < 10$ , we observe a characteristic easy-plane magnetization behavior. Furthermore, the evolution of the samples remanent magnetic domain structures with magnetic field history was explored by magnetic force microscopy. It was found that the remanent domain configuration can be gradually transformed from stripes to bubbles after applying different magnetic field sequences along the out-of-plane direction. This magnetic transition was identified by mapping out the density of the domains as a function of reduced field  $h_m$  and  $N$ . The resulting MFM data shows the magnetic transition with the occurrence of a region of a high-density bubble domain remanent state for  $0.70 \leq h_m \leq 0.85$  and

$18 \leq N \leq 20$ . The domain density in this region is significantly enhanced to  $\sim 2300$  domains/ $100 \mu\text{m}^2$ . The present work provides therefore a feasible approach for manipulating magnetic domains in Co/Pt multilayer film by finely adjusting the magnitude of the previously applied external magnetic field strength and the energetic landscape of the system. Furthermore, it is shown that the evolution of the domain structure can be controlled, which provides the possibility of manipulating magnetic domains with the applied field, for possible applications in spin-electronic or logic devices. Lastly, the demonstrated feasibility of tuning  $r$  and  $D$  by changing the number of Co/Pt repetitions, while at the same time keeping their morphology constant, may resemble a lithographic patterning process for creating two-dimensional dot or anti-dot lattices of varying dimensions. As for the samples presented here, the periodicity of the magnetic modulation as well as the modulation itself can be tuned and controlled by the strength of the external applied field and its orientation. This novel approach of all-magnetic patterning can prove useful in order to fabricate novel devices such as magnonic crystals [70]. Therefore, the thick Co/Pt multilayer systems presented here could constitute a relevant building block to be employed in magnonic devices in order to achieve specific and field-reconfigurable spin wave propagation and dispersion relations. Given the generality of our observations we expect that our findings might extend to many different ferromagnetic materials that exhibit a strong competition between long- and short-range interactions.

## ACKNOWLEDGMENTS

L. F. is thankful to Andreas Berger, Sven Stienen and Jürgen Lindner for fruitful discussions as well as to Kay Potzger for the support with experimental facilities. Part of the work was carried out with the support of CEITEC Nano Research Infrastructure (ID LM2015041, MEYS CR, 2016–2019), CEITEC Brno University of Technology. This work has received funding from the European Union’s Horizon 2020 research and innovation program under the Marie Skłodowska-Curie and it is co-financed by the South Moravian Region under grant agreement No. 665860.

## Figure Captions:

Fig. 1 (color online) (a) XRR  $\omega/2\theta$  scans for different samples with Co/Pt repetitions  $6 \leq N \leq 30$ . The inset shows a schematic of the layer growth sequence for the sample type explored in this study. (b) XRD  $\theta/2\theta$  measurements of the same samples as in (a): each scan has been normalized to the intensity of its Si (400) substrate peak. (c) XRD  $\theta/2\theta$  scan for the sample  $N = 30$ , which shows only Pt (111), Co/Pt\*<sup>1</sup> and its satellite peaks  $n$ , as well as the corresponding second order diffraction peaks, in addition to the Si (200) and Si (400) substrate signals. The indexing in (c) serves as reference for the scans displayed in (b).

Fig. 2 (color online) (a) Average total thickness of the single Co/Pt bilayer  $\bar{t}_{\text{Co+Pt}}$  vs.  $N$  as obtained from XRR measurements. The (red) dashed line indicates the nominal  $t_{\text{Co+Pt}} = 3.6$  nm. (b) Average out-of-plane interplanar distance  $\bar{d}_{\text{Co+Pt}}$  of the Co/Pt heterostructure vs.  $N$ . The (blue) dashed line and the (red) dotted line indicate the Pt (111) and Co (0002) interplanar distances, respectively. (c) FWHM of the rocking curve measurements performed at the Pt (111) diffraction angle as a function of  $N$ . (d) FWHM of the rocking curve measurements performed at the Co/Pt\* heterostructure diffraction peak<sup>1</sup> as a function of  $N$ .

Fig. 3 (color online) (a)-(m) VSM room temperature magnetization reversal curve measurements with the applied field along the IP (black) and OOP (red) directions for the entire set of  $[\text{Co/Pt}]_N$  samples. The data are normalized to its maximum value  $M_{\text{max}}$  in each case. (n)-(q) Zoomed-in view of the OOP magnetization reversal curve for four selected samples with (n)  $N = 6$ , (o) 14, (p) 22 and (q) 30. (r)-(s)  $N$ -dependence of the OOP-saturation magnetic field  $\mu_0 H_s^{\text{OOP}}$  (red circles), the nucleation magnetic field  $\mu_0 H_n^{\text{OOP}}$  (light blue triangles) and IP saturation magnetic field  $\mu_0 H_s^{\text{IP}}$ .

Fig. 4 (color online)  $\Delta M/M_{\text{max}}$  (color-coded) maps as a function of field angle  $\beta$  and strength  $\mu_0 H$  measured for different samples with  $8 \leq N \leq 30$  as indicated in each map. The scale (color code) is defined in the figure.  $\beta = 0^\circ$  corresponds to  $H$  applied along the surface normal (OOP),  $\beta = 90^\circ$  refers to IP field orientation. The  $\Delta M/M_{\text{max}}$  values are defined as the difference between the ascending and descending branches of the magnetization curves.

Fig. 5 (color online)  $\Delta M/M_{\max}$  (color-coded) maps as a function of field strength  $\mu_0 H$  and number of Co/Pt bilayers  $N$  for applied field angle values (a)  $\beta = 0^\circ$  and (b)  $90^\circ$ . The scale (color code) is defined in the figure.

Fig. 6 (color online) Remanent MFM images recorded after the OOP demagnetization process as a function of  $N$ . The same color scale (gray code) is used for all the images, as defined in the figure for the sample  $N = 8$ . The insets display the normalized to the maximum two-dimensional fast Fourier transform of the MFM image shown in the same figure. The same scale (color code) is used for all the 2D-FFT images, as defined in the inset of the figure for the sample  $N = 8$ .

Fig. 7 (color online) Remanent MFM images measured after the IP demagnetization process for the samples with (a)  $N = 30$  and (b)  $N = 10$ . The scale (gray code) is defined in each figure. (c) shows the magnetic domain periodicity  $\lambda$  as a function of  $N$  (black squares) together with the results of the fitting procedure by a power-law function. (d) displays the  $N$ -dependence of the in-plane remanence ratio  $M_r^{IP}/M_{\max}^{IP}$  together with schematics indicating the remanent magnetic state in the three different regions.

Fig. 8 (color online) VSM room temperature magnetization reversal curve measurements along the OOP field direction for the sample with  $N=20$ . Hereby, the magnetization is normalized to the maximum value  $M_{\max}$ , whereas the magnetic field values are divided by  $\mu_0 H_S^{\text{OOP}}$ . In (a) the full VSM major loop is displayed with the inset showing the remanent magnetic domain configuration after the field  $h_m = 1.6 \times \mu_0 H_S^{\text{OOP}}$  well above saturation was applied. (b)-(h) show VSM minor loops where the externally applied magnetic field does not exceed  $h_m = \gamma \times \mu_0 H_S^{\text{OOP}}$ , with  $\gamma = [1.00(\text{black, b}), 0.95(\text{magenta, c}), 0.90(\text{blue, d}), 0.85(\text{gold, e}), 0.80(\text{blue, f}), 0.75(\text{royal, g}), 0.70(\text{green, h})]$ . Each inset shows the remanent magnetic domain configuration after the corresponding  $h_m$  was applied. Moreover, the complete magnetization reversal curve displayed in (a) is also plotted as dashed (red) line in (b-h) for reference in the background. The left inset in (f) shows a zoomed area of the MFM images depicted on the right-hand side, with a hexagonal-like lattice illustrated schematically.

Fig. 9 (color online) Remanent MFM images measured as a function of  $N$  and the reduced magnetic field strength  $h_m$ . Each MFM image covers a  $2 \times 2 \mu\text{m}^2$  area. The scale (grey code) is



the same as in Figs. 6 and 7. The number at the corner of each MFM image refers to the magnetic domain density  $\rho$  (number of domains per 100 microns square) at remanence (see main text).

Fig. 10 (color online) (a)-(i) Normalized remanent magnetic domain density  $\rho$  as a function of  $h_m$  and for  $14 \leq N \leq 30$ . The (red) solid lines represent the least-squares fits to Eq. (1) for each of the sample data sets. The insets in each figure display  $3 \times 3 \mu\text{m}^2$  MFM images, which were measured after applying  $h_m = 1.6$ . (j) reduced magnetic field corresponding to the maximum remanent magnetic domain density  $h_m[\rho_{\text{max}}]$  as a function of  $N$ . The (red) dashed line indicates the weighted average.

Fig. 11 (color online) (a) Color-coded map of the magnetic domain density at remanence as a function of  $h_m$  and  $N$ . The scale (color code) is defined in (c). (b) Maximum domain density  $\rho_{\text{max}}$  as a function of  $N$ . (c) Color-coded map of the maximum magnetic domain density at remanence as a function of  $N$  and the thickness of the individual cobalt layers  $t_{\text{Co}}$ . The data corresponding to  $N = 50$  is adapted from [49], whereas the data for ( $31 \leq N \leq 50$ ,  $t_{\text{Co}} = 3.0 \text{ nm}$ ) are a linear interpolation based on both studies. The insets illustrate two areas covered by only bubble-like domains for the samples  $N = 30$  (inset I) and  $N = 20$  (inset II), with the arrows referring to the local orientation of the magnetization either up (yellow arrow and black color) or down (green arrow and white color). The z-dimension has been artificially created while assuming the absence of depth dependence domain shape modulation. (d) Average nearest neighbor distance between bubbles  $D$ , plotted as a function of bubble radius  $r$ . The schematic inset shows the definition of the quantities plotted in (d). The number accompanying the data-points in the plot is the repetition number  $N$  of Co/Pt multilayer system.

FIGURE 1

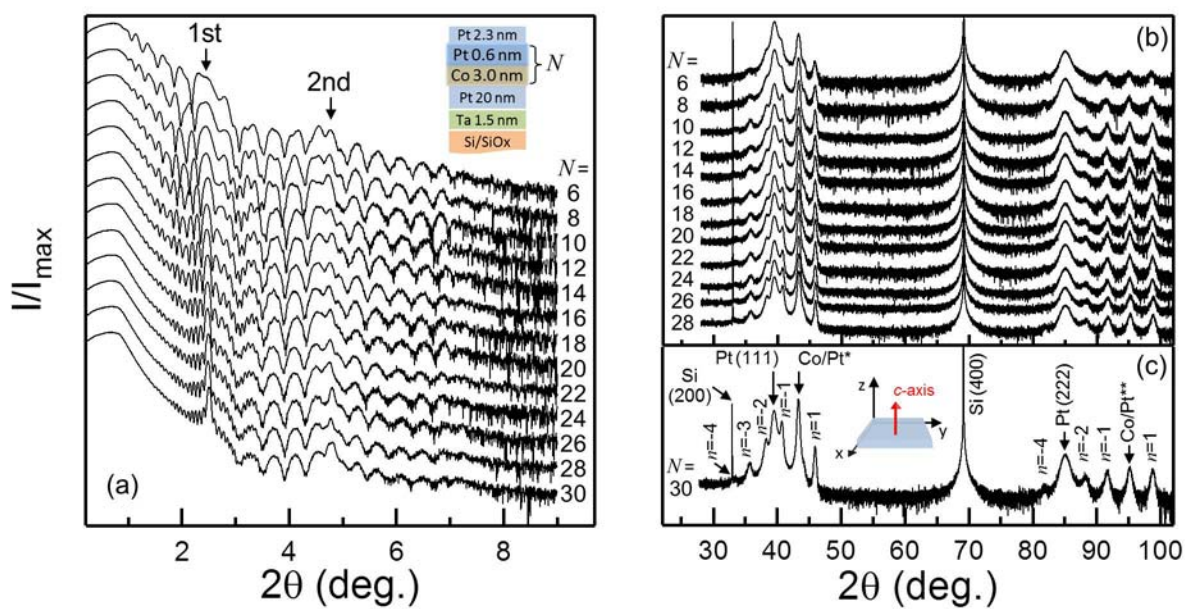


# FIGURE 2

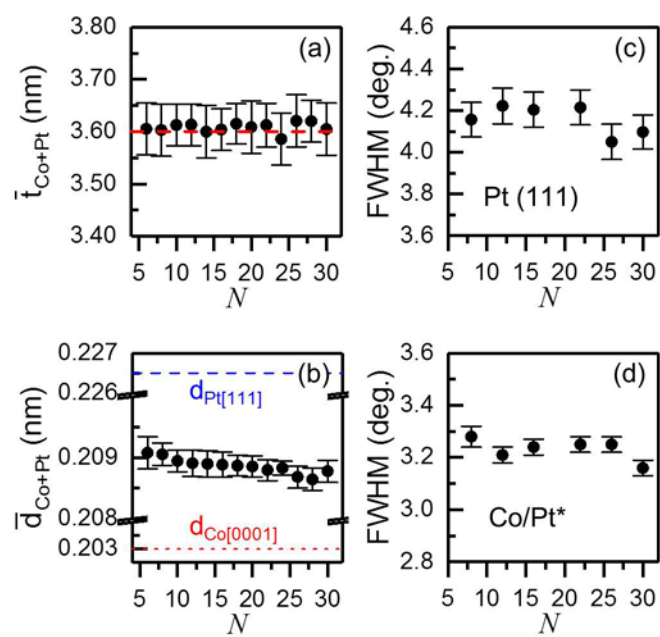


FIGURE 3

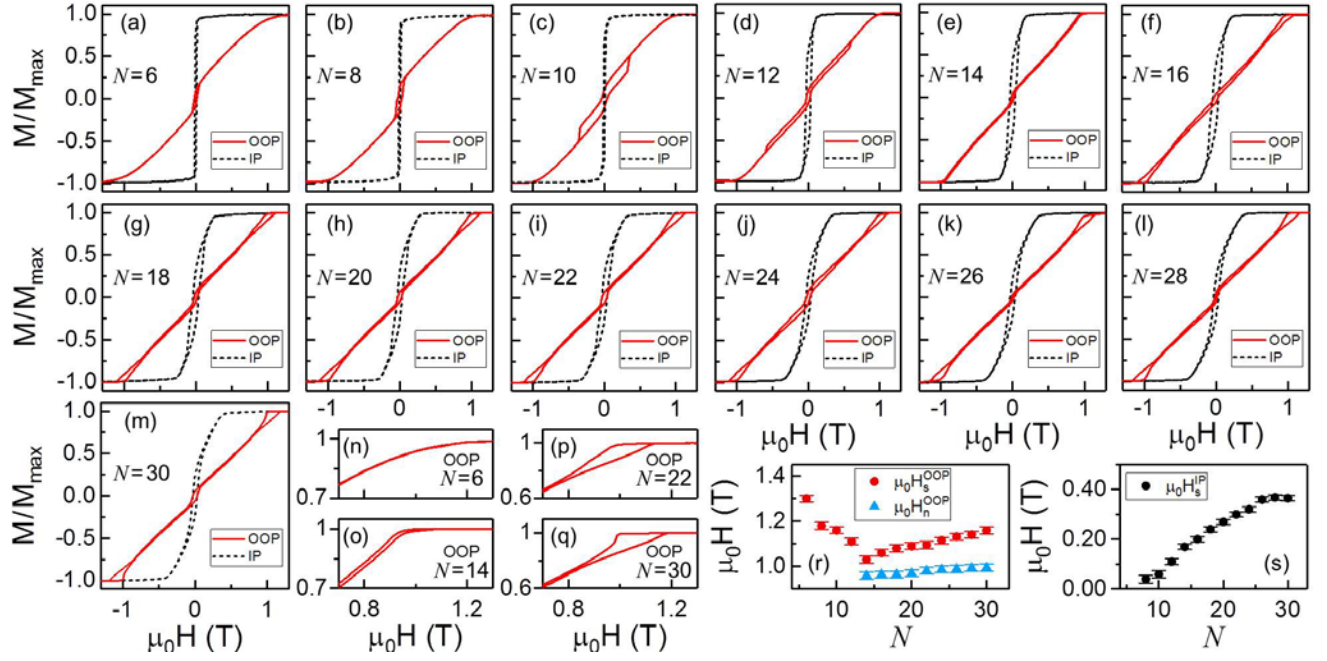


FIGURE 4

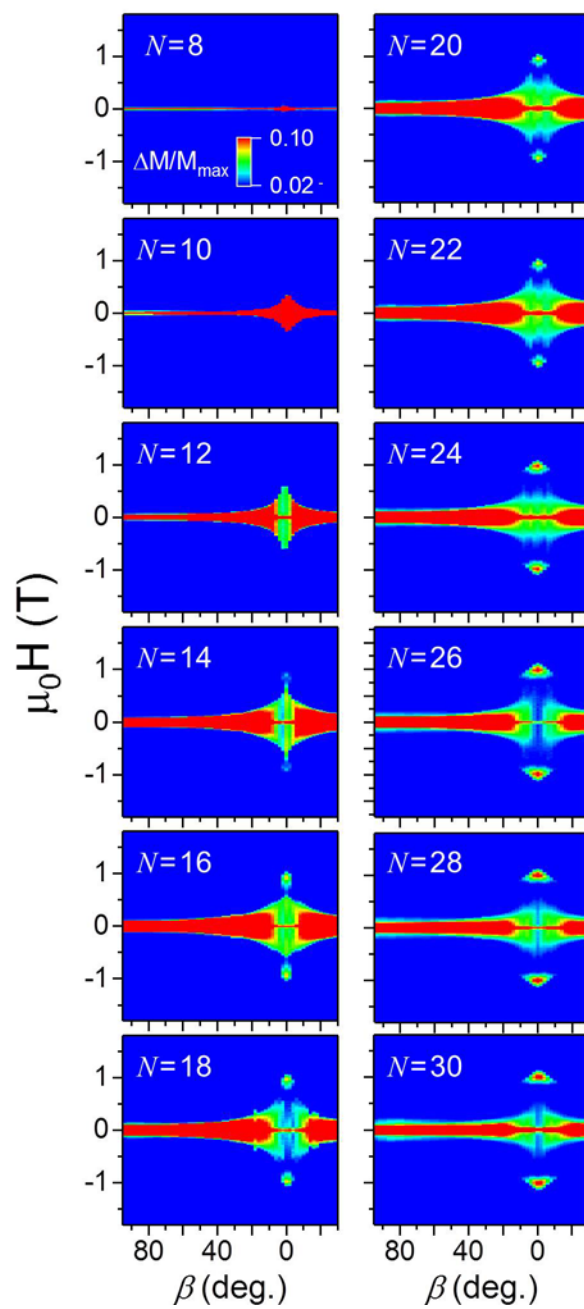
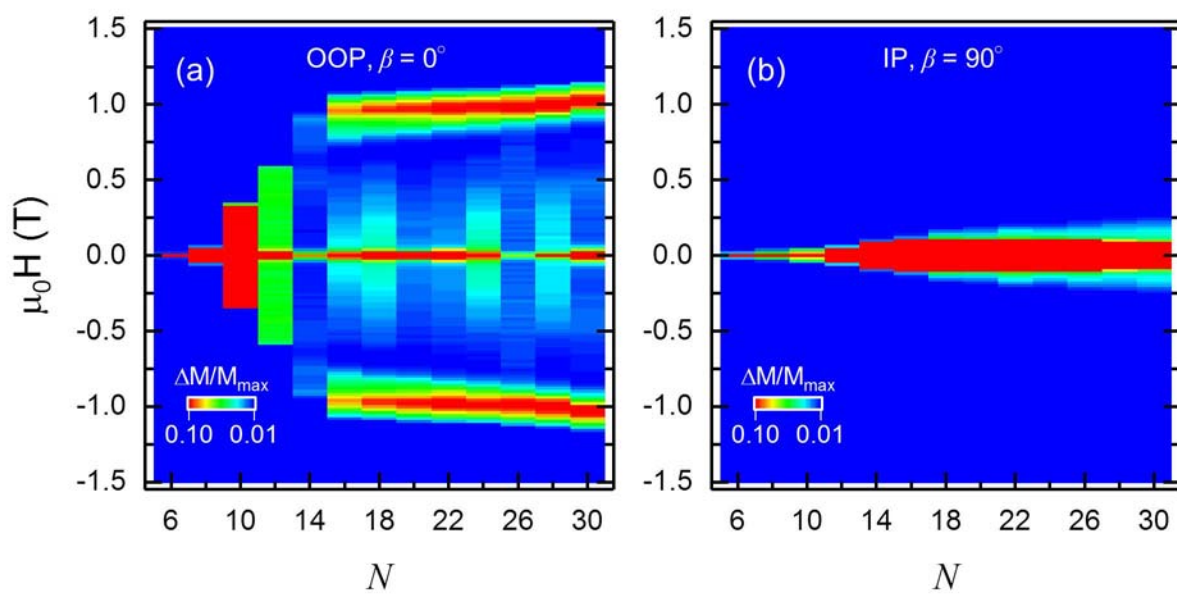


FIGURE 5



# FIGURE 6

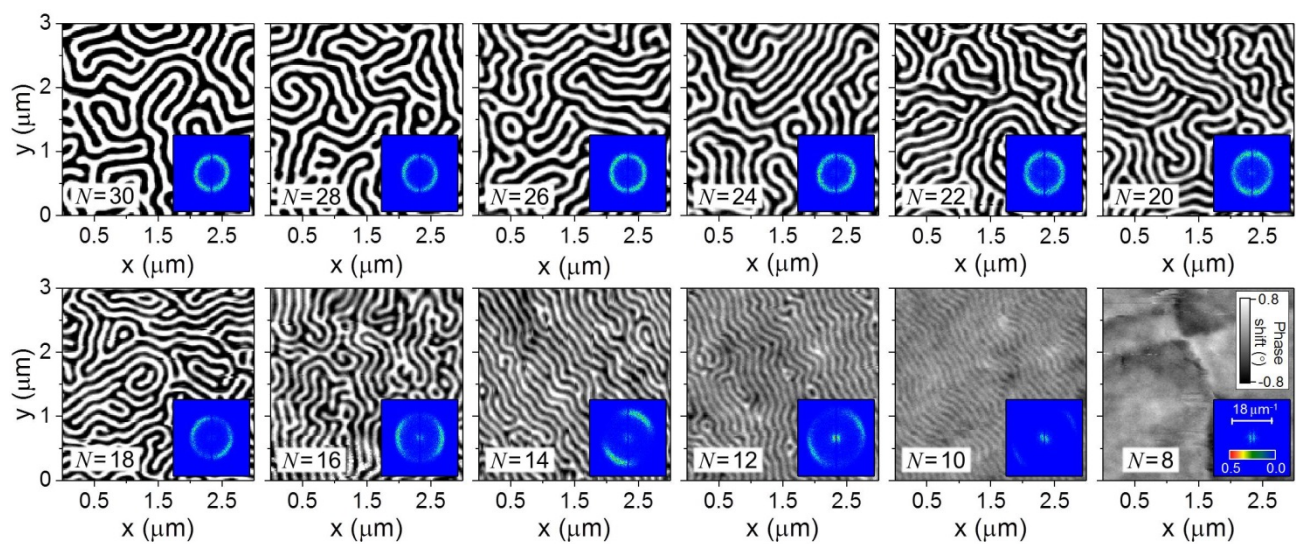
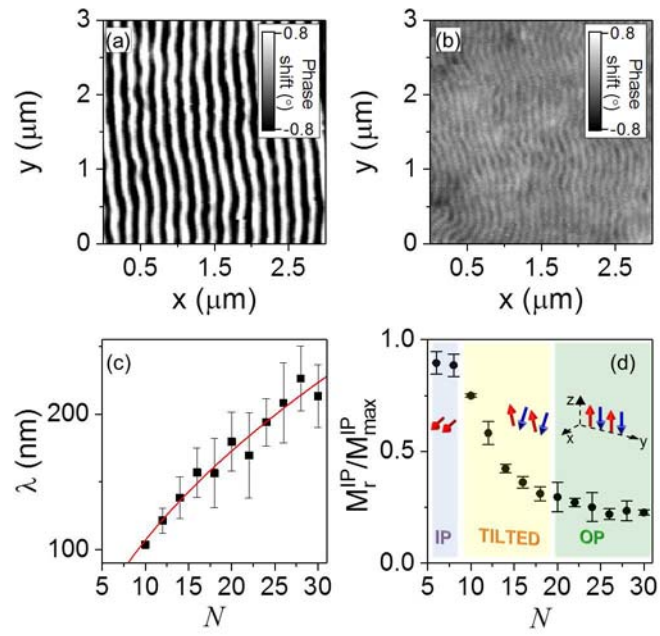


FIGURE 7





# FIGURE 8

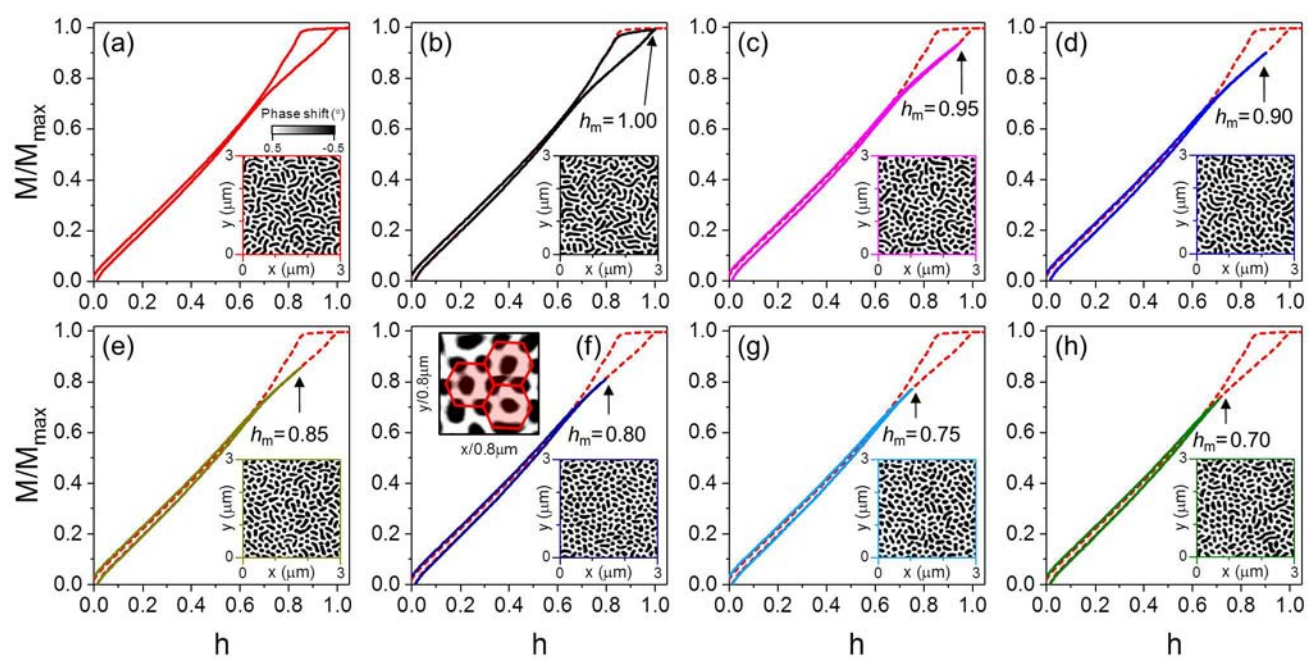


FIGURE 9

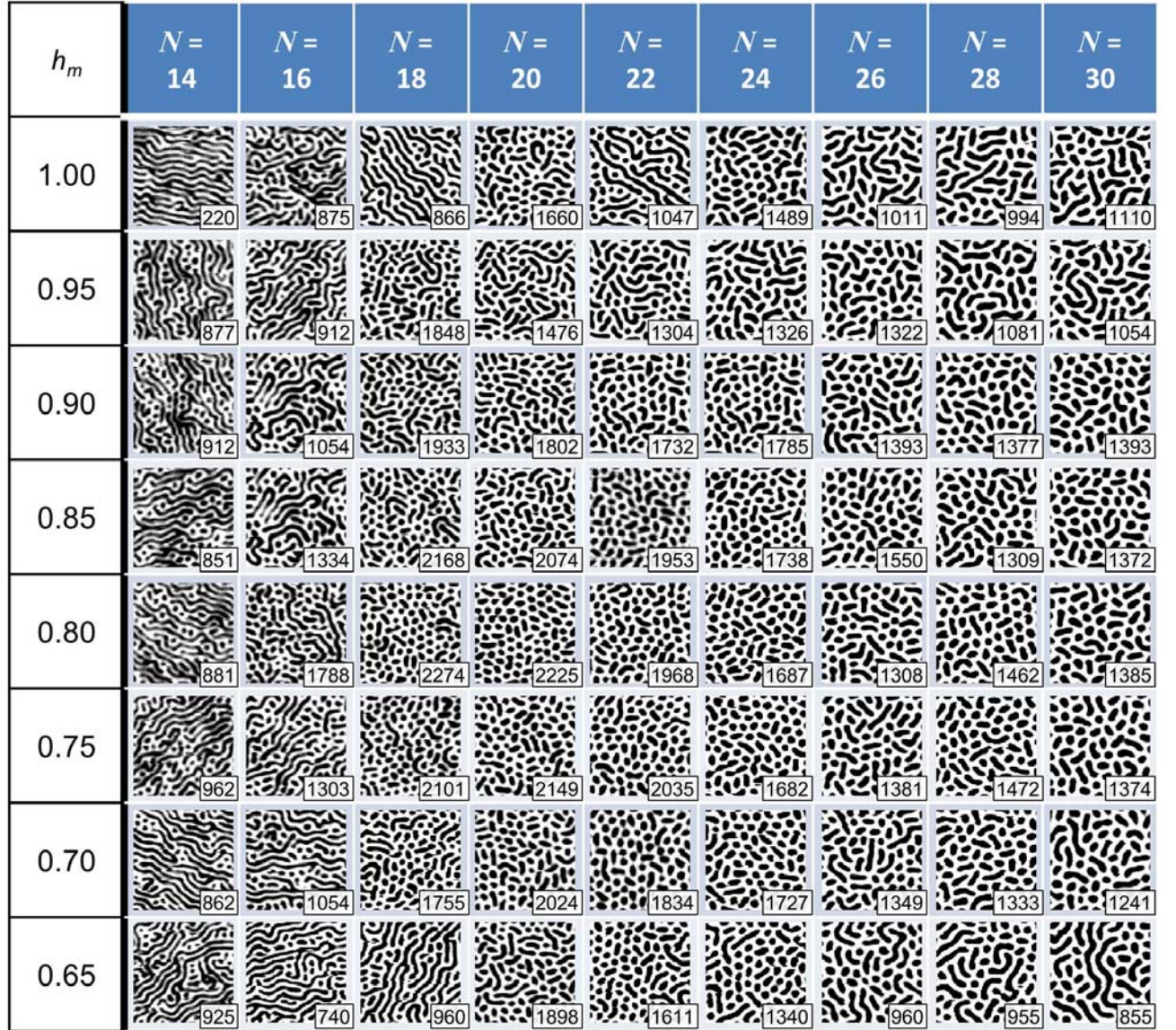
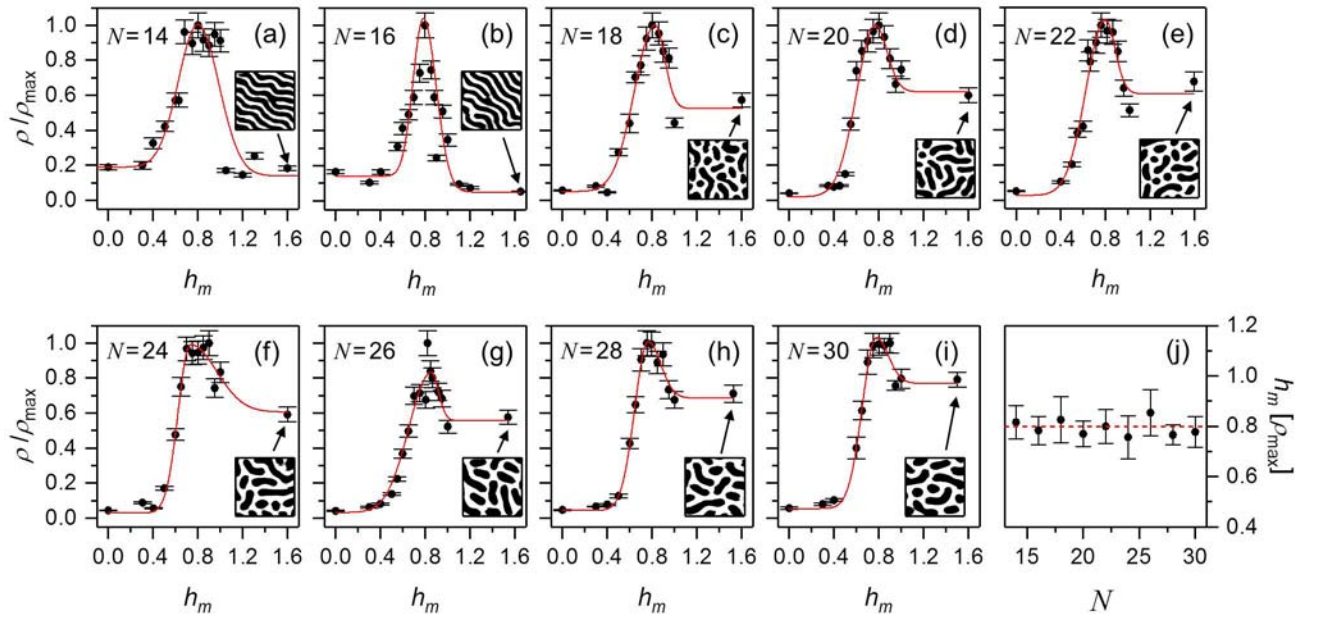
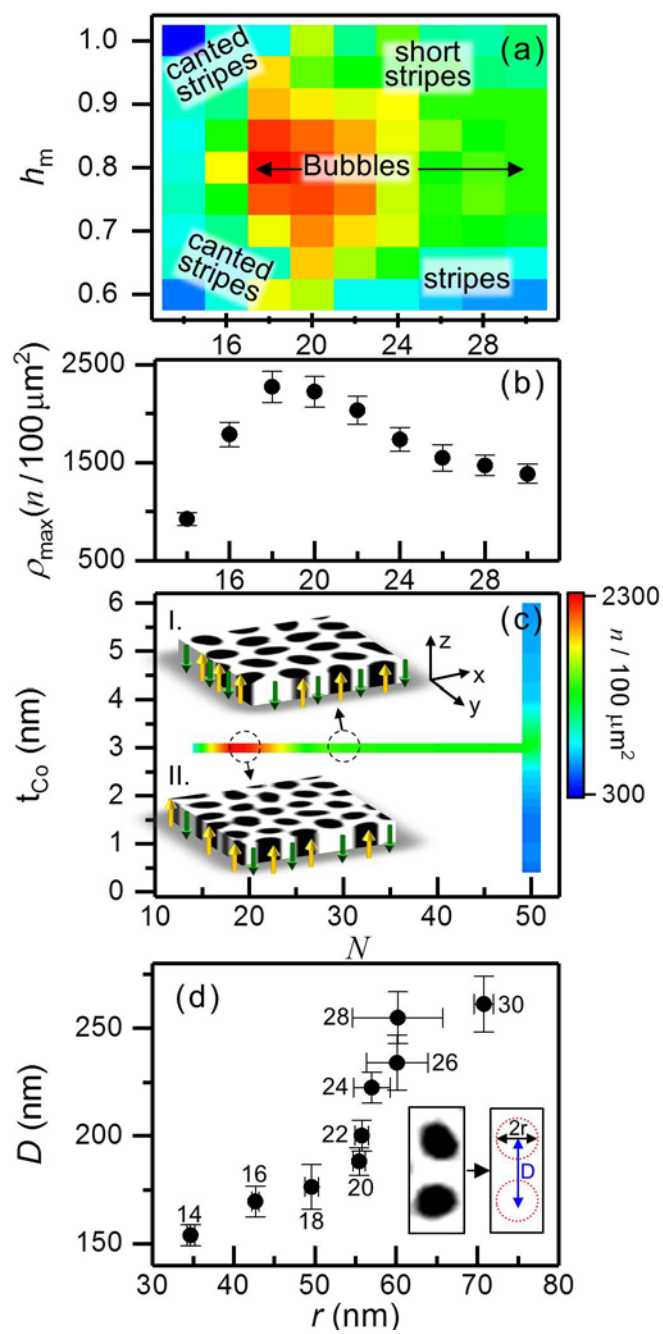


FIGURE 10





# FIGURE 11



## References

- [1] C. Kittel, Rev. Mod. Phys. **21**, 541-583 (1949); C. Kittel and J. K. Galt, Solid State Phys. **3**, 437-565 (1956).
- [2] A. Hubert and R. Schäfer, Magnetic Domains (Springer-Verlag Berlin Heidelberg, 1998).
- [3] R. Allenspach, M. Stampanoni, and A. Bischof, Phys. Rev. Lett. **65**, 3344 (1990).
- [4] R. Allenspach J. Magn. Magn. Mat. **129**, 160-185 (1994).
- [5] D. M. Donnet, K. M. Krishnan, and A. Yajima, J. Phys. D **28**, 1942 (1996).
- [6] M. Hehn, S. Padovani, K. Ounadjela, and J. P. Bucher, Phys. Rev. B **54**, 3428 (1996).
- [7] M. Hehn, K. Cherifi-Khodjaoui, K. Ounadjela, J. P. Bucher, and J. Arabski, J. Magn. Magn. Mat. **165**, 520-523 (1997).
- [8] M. Hehn, K. Ounadjela, R. Ferrè, W. Grange, and F. Rousseaux, Appl. Phys. Lett. **71**, 2833 (1997).
- [9] V. Gehanno, Y. Samson, A. Marty, B. Gilles, and A. Chamberod, J. Magn. Magn. Mater. **172**, 26-40 (1997).
- [10] J. U. Thiele, L. Folks, M. F. Toney, and D. K. Weller, J. Appl. Phys. **84**, 5686 (1998).
- [11] M. Demand, S. Padovani, M. Hehn, K. Ounadjela, and J. P. Bucher, J. Magn. Magn. Mat. **247**, 147-152 (2002).
- [12] A. K. Suszka, A. Etxebarria, O. Idigoras, D. Cortés-Ortuño, P. Landeros, and A. Berger, Appl. Phys. Lett. **105**, 222402 (2014).
- [13] L. Fallarino, O. Hovorka, and A. Berger, Phys. Rev. B **94**, 064408 (2016).
- [14] O. Hellwig, T. L. Kirk, J. B. Kortright, A. Berger, and E. E. Fullerton, Nat. Mat. **2**, 112 (2003).
- [15] O. Hellwig, A. Berger, and E. E. Fullerton, Phys. Rev. Lett. **91**, 197203 (2003).
- [16] J. E. Davies, O. Hellwig, E. E. Fullerton, G. Denbeaux, J. B. Kortright, and K. Liu, Phys. Rev. B **70**, 224434 (2004).
- [17] O. Hellwig, A. Berger, J. B. Kortright, and E. E. Fullerton, J. Magn. Magn. Mat. **319**, 13-55 (2004).
- [18] R. Sbiaa, Z. Bilin, M. Ranjbar, H. K. Tan, S. J. Wong, S. N. Piramanayagam, and T. C. Chong, J. Appl. Phys. **107**, 103901 (2010).

- [19] L. Belliard, J. Miltat, V. Kottler, V. Matht, C. Chappert, and T. Valet, J. Appl. Phys. **81**, 5315 (1997).
- [20] M. Labrune and A. Thiaville, Eur. Phys. J. B **23**, 17-28 (2001).
- [21] C. Bran, A. B. Butenko, N. S. Kiselev, U. Wolff, L. Schultz, O. Hellwig, U. K. Rößler, A. N. Bogdanov, and V. Neu, Phys. Rev. B **79**, 024430 (2009).
- [22] J. L. Archer, L. Tocci, P. K. George, and T. T. Chen, IEEE Trans. Magnetics **8**, 695-700 (1972).
- [23] A. H. Eschenfelder, *Magnetic Bubble Technology Vol. 14* (Springer Berlin, 1980).
- [24] T. H. O'Dell, Rep. Prog. Phys. **49**, 589 (1986).
- [25] K. Kudo, M. Suzuki, K. Kojima, T. Yasue, N. Akutsu, W. A. Diño, H. Kasai, E. Bauer, and T. Koshikawa, Phys.: Condens. Matter. **25**, 395005 (2013).
- [26] N. Ogawa, W. Koshibae, A. J. Beekman, N. Nagaosa, M. Kubota, M. Kawasaki, and Y. Tokura, PNAS **112**, 8977 (2015).
- [27] C. Banerjee, P. Gruszecki, J. W. Klos, O. Hellwig, M. Krawczyk, and A. Barman, Phys. Rev B **96**, 024421 (2017).
- [28] I. S. Camara, S. Tacchi, L. –C. Garnier, M. Eddrief, F. Fortuna, G. Carlotti, and M. Marangolo, J. Phys.: Condens. Matter **29**, 465803 (2017).
- [29] L. Landau and E. Lifshitz, Phys. Z. Sowjetunion **8**, 153 (1935).
- [30] C. Kittel, Phys. Rev. **70**, 965 (1946).
- [31] C. Kooy and U. Enz, Philips Res. Rep. **15**, 7 (1960).
- [32] M. W. Muller, Phys. Rev. **122**, 1485 (1961); W. F. Brown, Jr., ibid. **124**, 1348 (1961).
- [33] A. A. Thiele, Bell Syst. Tech. J. **48**, 3287 (1969).
- [34] A. H. Bobeck and E. Della Torre, *Magnetic Bubbles* (North-Holland Publishing Company, Amsterdam, 1975).
- [35] J. Davies, R. Clover, B. Lieberman, and D. Rose, IEEE Trans. Magn. **16**, 1106 (1980).
- [36] P. Pavan, R. Bez, P. Olivo, and E. Zanoni, Proc. IEEE **85**, 8 (1997).
- [37] P. Molho, J. L. Porteseil, Y. Souche, J. Gouzerh, and J. C. S. Levy, J. Appl. Phys. **61**, 4188 (1987).
- [38] M. Seul and C. A. Murray, Science **262**, 558 (1993).
- [39] M. Seul and D. Andelman, Science **267**, 476 (1995).

- [40] H. Nakajima, A. Kotani, K. Harada, Y. Ishii, and S. Mori, Phys. Rev. B **94**, 224427 (2016).
- [41] L. Sun, R. X. Cao, B. F. Miao, Z. Feng, B. You, D. Wu, W. Zhang, An Hu, and H. F. Ding, Phys. Rev. Lett. **110**, 167201 (2013).
- [42] W. B. Zeper, F. J. A. M. Greidanus, P. F. Carcia, IEEE Trans. Magn. **25**, 3764 (1989).
- [43] W. B. Zeper, H. W. van Kesteren, B. A. J. Jacobs, J. H. M. Spruit, and P. F. Carcia, J. Appl. Phys. **70**, 2264 (1991).
- [44] Y. Yafet and E. M. Gyorgy, Phys. Rev. B **38**, 9145 (1988).
- [45] F. J. A. den Broeder, D. Kuiper, A. P. van de Mosselaer, and W. Hoving, Phys. Rev. Lett. **60**, 2769 (1988).
- [46] C. -J. Lin, G. L. Gorman, C. H. Lee, R. F. C. Farrow, E. E. Marinero, H. V. Do, H. Notarys, and C. J. Chien, J. Magn. Magn. Mat. **93**, 194-206 (1991).
- [47] M. T. Johnson, P. J. H. Bloemen, F. J. A. den Broeder and J. J. de Vriest, Rep. Prog. Phys. **59**, 1409 (1996).
- [48] J. Gao, S. Tang, Y. Li, W. Xia, T. Tang, and Y. Du., J. of Appl. Phys. **112**, 073913 (2012).
- [49] K. Chesnel, A. S. Westover, C. Richards, B. Newbold, M. Healey, L. Hindman, B. Dodson, K. Cardon, D. Montealegre, J. Metzner, F. Samad, L. Fallarino, B. Böhm, T. Schneider, and O. Hellwig, submitted to Phys. Rev. B.
- [50] A. Westover, K. Chesnel, K. Hatch, P. Salter, and O. Hellwig, J. Magn. Magn. Mater. **399**, 164 (2016).
- [51] N. Nakajima, T. Koide, T. Shidara, H. Miyauchi, H. Fukutani, A. Fujimori, K. Iio, T. Katayama, M. Nývlt, and Y. Suzuki, Phys. Rev. Lett. **81**, 5229 (1998).
- [52] B. N. Engel, C. D. England, R. A. Van Leeuwen, M. H. Wiedmann, and C. M. Falco, Phys. Rev. Lett. **67**, 1910 (1991).
- [53] J.-W. Lee, J.-R. Jeong, S.-C. Shin, J. Kim, S.-K. Kim, Phys. Rev. B **66**, 172409 (2002).
- [54] M. Kisielewski, A. Maziewski, M. Tekielak, J. Ferré, S. Lemerle, V. Mathet, and C. Chappert, J. Magn. Magn. Mat. **260**, 231-243 (2003).
- [55] R. Fromter, H. Stillrich, C. Menk, and H. P. Oepen, Phys. Rev. Lett. **100**, 207202 (2008).
- [56] Z. Malek, V. Kambersky, Czech. J. Phys. **8**, 416 (1958).

- [57] R. Allenspach and M. Stampanoni, in *Magnetic Surfaces, Thin Films, and Multilayers*, edited by S. S. P. Parkin et al., MRS Symposia Proceedings No. 231 (Materials Research Society, Pittsburgh, 1992), p.17.
- [58] W. Jiang, G. Chen, K. Liu, J. Zang, S. G. E. te Velthuis, and A. Hoffmann, *Phys. Rep.* **704**, 1 (2017).
- [59] M. Birkholz, *Thin Film Analysis by X-Ray Scattering* (Wiley, New York, 2006).
- [60] O. Hellwig, S. Maat, J. B. Kortright, and E. E. Fullerton, *Phys. Rev. B* **65**, 144418 (2002).
- [61] O. Hellwig, G. P. Denbeaux, J. B. Kortright, and E. E. Fullerton, *Physica B* **336**, 136 (2003).
- [62] A. Berger, A. W. Pang, and H. Hopster, *Phys. Rev. B* **52**, 1078 (1995).
- [63] L. Fallarino, B. J. Kirby, M. Pancaldi, P. Riego, A. L. Balk, C. W. Miller, P. Vavassori, and A. Berger, *Phys. Rev. B* **95**, 134445 (2017).
- [64] L. Fallarino, P. Riego, B. J. Kirby, C. W. Miller, and A. Berger, *Materials* **11**, 251 (2018).
- [65] S. Tacchi, S. Fin, G. Carlotti, G. Gubbiotti, M. Madami, M. Barturen, M. Marangolo, M. Eddrief, D. Bisero, A. Rettori, and M. G. Pini, *Phys. Rev. B* **89**, 024411 (2014).
- [66] J. Muller, *J. Appl. Phys.* **38**, 2413 (1967).
- [67] S. A. Montoya, S. Couture, J. J. Chess, J. C. T. Lee, N. Kent, M. –Y. Im, S. D. Kevan, P. Fischer, B. J. McMorran, S. Roy, V. Lomakin, and E. E. Fullerton, *Phys. Rev. B* **95**, 224405 (2017).
- [68] S. A. Montoya, S. Couture, J. J. Chess, J. C. T. Lee, N. Kent, D. Henze, S. K. Sinha, M. –Y. Im, S. D. Kevan, P. Fischer, B. J. McMorran, V. Lomakin, S. Roy, and E. E. Fullerton, *Phys. Rev. B* **95**, 024415 (2017).
- [69] F. W. F. Dorleijn, W. F. Druyvesteyn, F. A. de Jonge, and H. M. W. Boolij, *IEEE Trans. Magn.* **7**, 355-358 (1971).
- [70] S. Neusser and D. Grundler, *Adv. Mater.* **21**, 2927 (2009).